



Article

# Effect of Nb and Mo Additions in the Microstructure/Tensile Property Relationship in High Strength Quenched and Quenched and Tempered Boron Steels

Irati Zurutuza<sup>1,2</sup>, Nerea Isasti<sup>1,2</sup>, Eric Detemple<sup>3</sup>, Volker Schwinn<sup>3</sup>, Hardy Mohrbacher<sup>4,5</sup>  and Pello Uranga<sup>1,2,\*</sup> 

- <sup>1</sup> Materials and Manufacturing Division, CEIT-Basque Research and Technology Alliance (BRTA), 20018 Donostia/San Sebastián, Basque Country, Spain; izurutuza@ceit.es (I.Z.); nisasti@ceit.es (N.I.)
- <sup>2</sup> Tecnun, Mechanical and Materials Engineering Department, Universidad de Navarra, 20018 Donostia/San Sebastián, Basque Country, Spain
- <sup>3</sup> AG der Dillinger Hüttenwerke, 66763 Dillingen/Saar, Germany; Eric.Detemple@dillinger.biz (E.D.); Volker.Schwinn@dillinger.biz (V.S.)
- <sup>4</sup> NiobelCon BV, 2970 Schilde, Belgium; hm@niobelcon.net
- <sup>5</sup> Department of Materials Engineering (MTM), KU Leuven, 3001 Leuven, Belgium
- \* Correspondence: puranga@ceit.es; Tel.: +34-943212800

**Abstract:** Recently, advanced thermomechanical hot rolling schedules followed by direct quenching are being developed in order to avoid reheating and quenching treatment after hot rolling to eliminate an energy and cost consuming step. The use of boron as an alloying element is a widely known practice in high strength medium carbon steels to increase the strength due its potential for delaying phase transformation and improving hardenability. In addition, a significant synergetic effect on hardenability could be reached combining B with microalloying elements (adding Nb, Mo or Nb-Mo). With the purpose of exploring the effect of microalloying elements and thermomechanical rolling schedule, laboratory thermomechanical simulations reproducing plate mill conditions were performed using ultra high strength steels micro-alloyed with Nb, Mo, and Nb-Mo. To that end, plane compression tests were performed, consisting of an initial preconditioning step, followed by several roughing and finishing deformation passes and a final quenching step. After fast cooling to room temperature, a tempering treatment was applied. In the present paper, the complex interaction between the martensitic microstructure, the tempering treatment, the addition of microalloying elements, and the resulting tensile properties was evaluated. For that purpose, an exhaustive EBSD quantification was carried out in both quenched as well as quenched and tempered states for all the steel grades and the contribution of different strengthening mechanisms on yield strength was analyzed. Highest tensile properties are achieved combining Nb and Mo, for both quenched (Q) and quenched and tempered states (Q&T), reaching yield strength values of 1107 MPa and 977 MPa, respectively. Higher tempering resistance was measured for the Mo-bearing steels, making the CMnNbMoB steel the one with the lowest softening after tempering. For CMnB grade, the yield strength reduction after tempering of about 413 MPa was measured, while for NbMo micro-alloyed steel, yield strength softening is considerably reduced to 130 MPa.

**Keywords:** martensite; Q + T steels; thermomechanical simulations; tensile properties; microalloying elements



**Citation:** Zurutuza, I.; Isasti, N.; Detemple, E.; Schwinn, V.; Mohrbacher, H.; Uranga, P. Effect of Nb and Mo Additions in the Microstructure/Tensile Property Relationship in High Strength Quenched and Quenched and Tempered Boron Steels. *Metals* **2021**, *11*, 29. <https://doi.org/10.3390/met11010029>

Received: 4 December 2020

Accepted: 23 December 2020

Published: 25 December 2020

**Publisher's Note:** MDPI stays neutral with regard to jurisdictional claims in published maps and institutional affiliations.



**Copyright:** © 2020 by the authors. Licensee MDPI, Basel, Switzerland. This article is an open access article distributed under the terms and conditions of the Creative Commons Attribution (CC BY) license (<https://creativecommons.org/licenses/by/4.0/>).

## 1. Introduction

In response to the market requirements for highest strength and good impact resistance, plate steels are usually quenched and tempered for a large variety of applications. Boron is an efficient microalloying element, commonly used in high strength medium carbon Quenched (Q) and quenched and tempered (Q&T) steels, in substitution for more

expensive elements. The addition of B increases strength, ensures hardenability, and promotes the formation of bainitic/martensitic microstructures. The pronounced segregation of B to the austenite grain boundary delays the nucleation of ferrite, which is the basis for its strong effect on hardenability [1–4]. In order to safeguard high efficiency in terms of hardenability, it is essential to maintain boron in solution and to avoid strong plastic deformation immediately before quenching. Avoiding traces of softer phases as well as establishing good homogeneity of the microstructure are essential for ensuring the best mechanical properties of the final product.

A synergetic effect on hardenability by combined alloying of B and Nb, as well as B and Mo [5–8] is widely reported in the literature. The potential loss of solute boron by formation of ferro-boron carbides ( $\text{Fe}_{23}(\text{C},\text{B})_6$ ) especially in the austenite grain boundary area is prevented by the formation of Nb or Mo carbides. Since Nb and Mo are well established as alloying elements in low carbon steel plates with yield strength levels above 500 MPa, the synergetic effect with boron is simultaneously provided. The major function of Nb addition is to strongly delay static recrystallization kinetics of the austenite, via solute drag and strain-induced precipitation [9,10]. This allows for the accumulation of deformation in austenite during finish rolling, resulting in grain size refinement of the final microstructure and thus improving mechanical properties [11,12]. Mo is usually added to steels when ultrahigh strength is requested. Through this addition, the formation of low-temperature transformation products such as bainite and martensite can be achieved [5]. It should be noted that molybdenum's hardenability mechanism is complementary to that of boron. Molybdenum also delays Nb precipitation in austenite while promoting a finer-sized and more copious NbC precipitate formation during or after transformation. This results in more pronounced precipitation hardening [11,13]. The effects of solute Nb and Mo on the austenite-to-ferrite transformation are similar. Both delay the phase transformation [14] and particularly obstruct pearlite formation [15], thus promoting bainite formation. This effect is standardly used when producing advanced high strength low alloy (HSLA) steels with increased toughness [16–18]. The synergetic effect of the addition of both elements has been primarily investigated in low carbon steels and ferritic/bainitic final microstructures ( $\text{C} < 0.10\%$ ) [12]. However, in high strength steels with an increased carbon content ( $\sim 0.15 \div 0.2\%$  C) and complex martensitic microstructures, a deeper understanding of these mechanisms is needed to optimize the synergetic effect of both elements. In this context, the present work will investigate the synergetic effect of B, Nb, and Mo in martensitic microstructures on the tensile properties.

Q and Q/T steels are usually produced by conventional quenching (CQ) routes in which the hot rolled plate is reheated to austenite in a separate process. Lately, the direct quenching (DQ) route after thermomechanical controlled processing is being used increasingly often. In the DQ process, the conditioned austenitic microstructure is subjected to high cooling rate immediately after hot rolling, promoting the transformation into martensite. The DQ route has economic and operational advantages over the CQ route, as it removes logistic bottlenecks and allows producing higher volumes of ultrahigh strength steel.

From a microstructural point of view, differences between the DQ and CQ processed products are expected. None withstanding that both products have martensitic microstructure, the difference is seen in the underlying prior austenite grain structure. In the CQ route the austenite grain morphology before quenching is equiaxed as cooling down and reheating result in a normalizing effect. The DQ process is quenching a conditioned austenite structure directly into martensite. Thus, austenite pancaking and heterogeneities related to recrystallization phenomena are being preserved in the martensitic microstructure. Austenite pancaking results in anisotropic mechanical properties of the final martensite particularly reflecting in differences of toughness and bendability between rolling and transverse direction [17]. Thermomechanical processing must be carefully designed to obtain an optimum pancaked austenite structure resulting in refined final grain size. Particular attention must be attributed to avoiding inhomogeneous austenite size and morphology as to ensure a good balance between tensile and toughness properties [19–21].

This paper analyzes the relationship between quenched martensite, quenched and tempered microstructures, and tensile properties in four different steels. To that end, tensile tests were performed for all the chemistries and both quenched and quenched and tempered states. In the current study, plane strain compression tests were performed for simulating DQ process. The impact of different strengthening mechanisms on the yield strength was calculated and a model able to evaluate the different strengthening contributions was developed for martensitic microstructures. The yield strength of martensitic microstructures composes of a combination of different strengthening mechanisms, such as solid solution hardening, grain size refinement, strain hardening and precipitation hardening. In addition, the role of carbon in solid solution is evaluated.

## 2. Materials and Methods

The chemical compositions of the laboratory cast steels are listed in Table 1. All the steels contain about 0.16% of carbon and 20 ppm of boron. They are alloyed with Ti to ensure the full effect of B. In addition to the plain CMnB steel, three different micro-alloyed steels are also included which are micro-alloyed with Nb, Mo and NbMo. The Nb and Mo contents are set to 0.026%Nb and 0.5%, respectively.

**Table 1.** Chemical composition of the studied steels (weight percent).

Steel	C	Si	Mn	Mo	Nb	B
CMnB	0.15	0.32	1.05	-	-	0.0022
CMnNbB	0.16	0.29	1.05	-	0.026	0.0019
CMnMoB	0.16	0.28	1.07	0.5	-	0.0022
CMnNbMoB	0.16	0.31	1.07	0.5	0.026	0.0018

Plane strain compression tests were performed in order to simulate the direct quenching and tempering treatments (see the thermomechanical schedule in Figure 1). For each chemistry, two laboratory tests were performed, one for simulating Q and another one for reproducing Q + T cycle. For that purpose, rectangular plane strain compression specimens were used (60 mm long, 30 mm wide, and 22 mm thick). Firstly, a preconditioning step consisting of soaking at 1200 °C for 10 min followed by a deformation pass ( $\epsilon = 0.2$  at  $1 \text{ s}^{-1}$ ) at 1140 °C was carried out to minimize the presence of coarse austenite grains. Afterwards, the samples were cooled down at a constant rate of  $1 \text{ °C/s}$  to room temperature. In a recently published work, and following the same hot working strategy, it was observed that the roughing and finishing passes were not able to refine the austenitic structure at reheating temperature [22]. Therefore, the preconditioning step was essential for ensuring a homogeneous and fine austenite prior to martensite transformation. Then, the plane compression specimens were reheated at 1200 °C for 10 min in order to ensure the dissolution of Nb in the CMnNbB and CMnNbMoB steels, followed by three roughing deformation passes ( $\epsilon = 0.2$  at  $2 \text{ s}^{-1}$ ) with an interpass time of 3 s at decreasing temperature in the 1140–1120 °C range. After a holding time of 360 s, the finishing passes were completed applying four deformation passes of 0.2 at  $5 \text{ s}^{-1}$  with an interpass time of 8 s in the 851 and 830 °C range. In order to simulate plate quenching conditions after the last deformation pass, an air–water mixture was employed. A cooling strategy of two steps was applied cooling down at  $30 \text{ °C/s}$  to 300 °C and then, at  $10 \text{ °C/s}$  down to room temperature. Finally, for the Q + T samples, a tempering treatment was performed at 600 °C for 15 min.

Due to sample/tool geometry and friction, a heterogeneous strain distribution through section is developed in the plane compression specimens [23]. Therefore, with the aim of avoiding strain gradients, the sample employed for microstructural characterization was cut from the central part of the plane compression specimen. The microstructures were characterized after etching in 2% Nital by optical microscopy (OM, LEICA DM15000 M, Leica microsystems, Wetzlar, Germany) and field-emission gun scanning electron microscopy (FEG-SEM, JEOL JSM-7100F, Tokyo, Japan). Carbide size and density measurements were carried out by FEG-SEM (considering equivalent diameter method). In all cases,

ization was cut from the central part of the plane compression specimen. The microstructures were characterized after etching in 2% Nital by optical microscopy (OM, LEICA DM15000 M, Leica microsystems, Wetzlar, Germany) and field-emission gun scanning electron microscopy (FEG-SEM, JEOL JSM-7100F, Tokyo, Japan). Carbide size and density measurements were carried out by FEG-SEM (considering equivalent diameter method). In all cases, between 200 and 450 particles were measured. Additionally, a more detailed microstructural characterization was performed using electron backscattered diffraction (EBSD), and crystallographic features were quantified for all the steel grades and both Q and Q + T states. For that purpose, the samples were polished down to 1  $\mu\text{m}$ , and the final polishing was performed with colloidal silica. Orientation imaging was carried out on the equipment with a camera NORDLYS II (Oxford Instruments, Abingdon, UK) and with an acquisition program and data analysis, OXFORD HKL CHANNEL 5 PREMIUM coupled to the JEOL JSM-7100F (FEG-SEM). A scan step size of 0.2  $\mu\text{m}$  was defined and the total scanned area was about 140  $\mu\text{m} \times 140 \mu\text{m}$ . The EBSD scans were analyzed by means of TSL OIM™ Analysis 5.31 software (TSL OIM Analysis 5.31 software (EDAX, Mahwah, NJ, USA)). The study of the fine precipitates was performed using a Transmission Electron Microscope (TEM, JEOL (TEM), JEOL Ltd., Tokyo, Japan) with a voltage of 200 kV and a beam diameter of 10  $\mu\text{m}$ . To that end, carbon extraction replicas were obtained, and precipitation analysis was carried out.

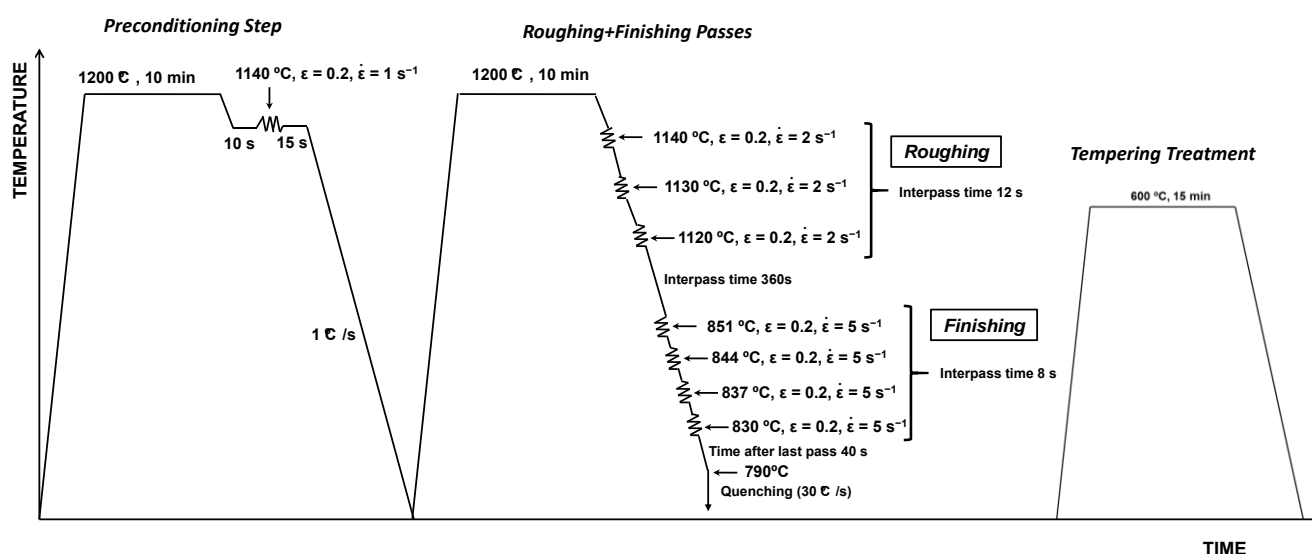


**Figure 1.** Schematics of the applied plane strain compression cycle.

Tensile tests were performed at room temperature in an Instron testing machine (INSTRON 9829R2 Instron Corp., Canton, MA, USA) under strain control (using an engineering strain rate of  $10^{-3} \text{ s}^{-1}$ ). Cylindrical tensile specimens with a gauge length of 17 mm and a diameter of 3 mm were machined from the central area of the plane strain compression specimens. Finally, Vickers hardness was also measured in all specimens, using a 1-Kg load. In the present study, the average value of six hardness measurements is reported.

### 3. Results and Discussion

#### 3.1. Microstructural Characterization

The microstructures obtained after quenching for all steel grades are shown in Figure 2 (optical microscopy) and Figure 3 (FEG-SEM). For the quenched state, fully martensitic microstructures are observed for all chemical compositions. Additionally, very fine carbides are also distinguished in the martensitic matrix (see Figure 3a–d), which are assumed to have formed by self-tempering during the final step of the accelerated cooling. The FEG-SEM images shown in Figure 3 allow us to compare the microstructures of the different alloys in quenched and quenched and tempered samples. The tempering treatment leads to the formation of the carbides, which, depending on the steel grade, differ considerably (see Table 2) in size and spatial distribution. For Mo containing steels  $\text{M}_2\text{C}$ ,  $\text{M}_6\text{C}$ , and  $\text{M}_{23}\text{C}_6$  type carbides were formed, whereas Nb forms only MC type carbides. It is obvious that molybdenum alloying results in finer-sized carbide particles as well as a higher particle density. In the tempered martensite, different type of carbides can be differentiated (see Figure 3), some of them pre-

siderably (see Table 2) in size and spatial distribution. For Mo containing steels MC, M<sub>6</sub>C, and M<sub>23</sub>C<sub>6</sub> type carbides were formed, whereas Nb forms only MC type carbides. It is obvious that molybdenum alloying results in finer-sized carbide particles as well as higher particle density. In the tempered martensite, different type of carbides can be differentiated (see Figure 3), some of them precipitate at the prior austenite grain boundaries and other carbides precipitate away from the austenite boundaries (within the prior austenite grains). Furthermore, the particle density of these carbides is lower considering the carbides located at prior austenite grain boundaries. Again, this is clearly more pronounced in molybdenum alloyed steels. The total carbide area fraction of both type of carbides increases with the alloy content. Molybdenum alloying has in this respect the dominating impact.

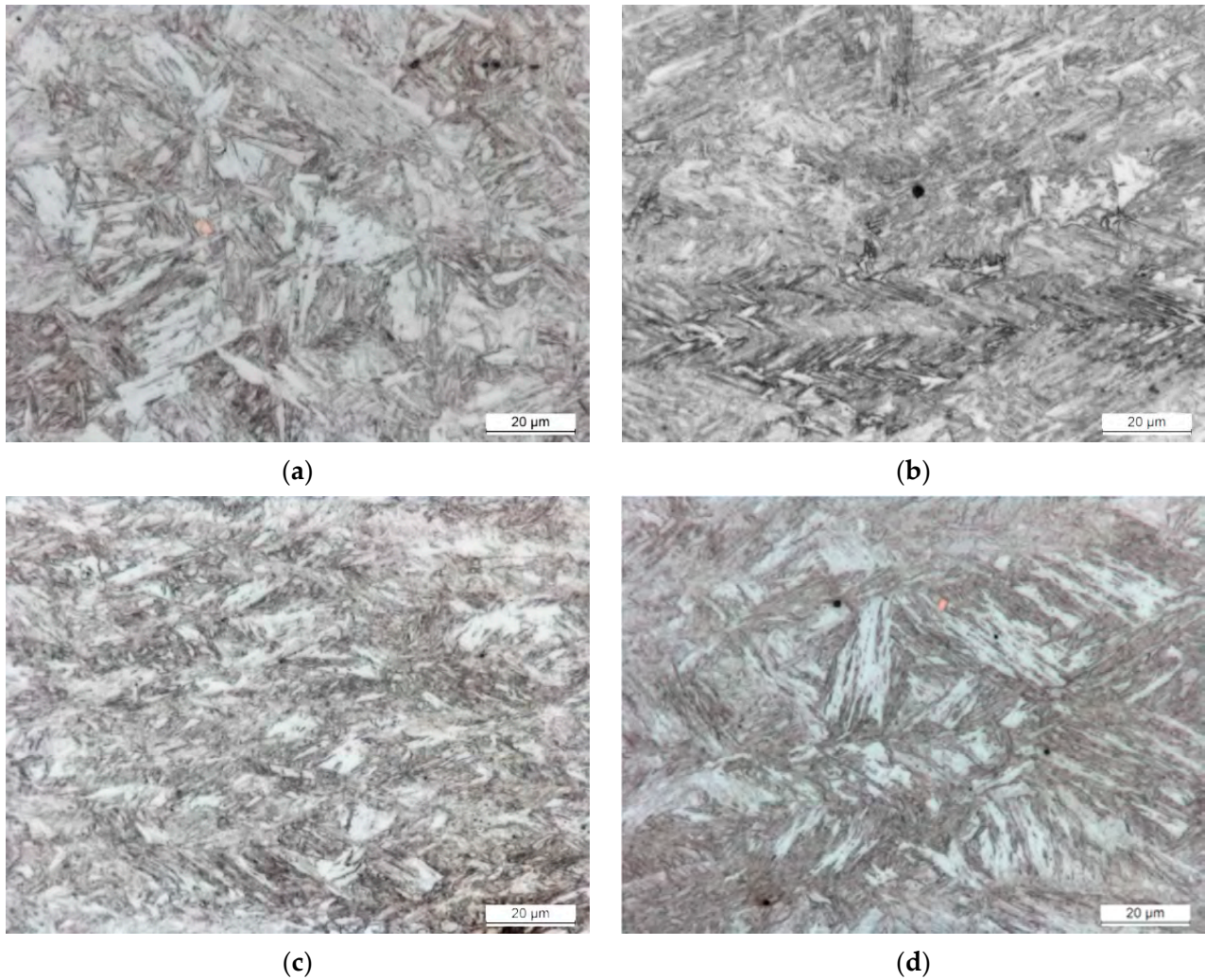


Figure 2. Optical micrographs after tempering (State) corresponding to (a) CMnB, (b) CMnNbB, (c) CMnMoB, and (d) CMnNbMoB steels.

Table 2. Measured mean carbide sizes and carbide densities considering both type of carbides (carbides located at prior austenite grain boundaries and inside prior austenite grains).

Steel	Carbides Located at Prior Austenite Grain Boundaries		Carbides Located Inside Prior Austenite Grains	
	Carbide Size (nm)	Area Fraction (%)	Carbide Size (nm)	Area Fraction (%)
CMnB	113.6 ± 3.9	0.18	103.8 ± 4.3	0.33
CMnNbB	115.3 ± 3.9	0.16	105.9 ± 4.4	0.41
CMnMoB	91.4 ± 5.4	0.29	59.4 ± 3.1	0.91
CMnNbMoB	80.4 ± 3.8	0.31	66.8 ± 2.9	1.26

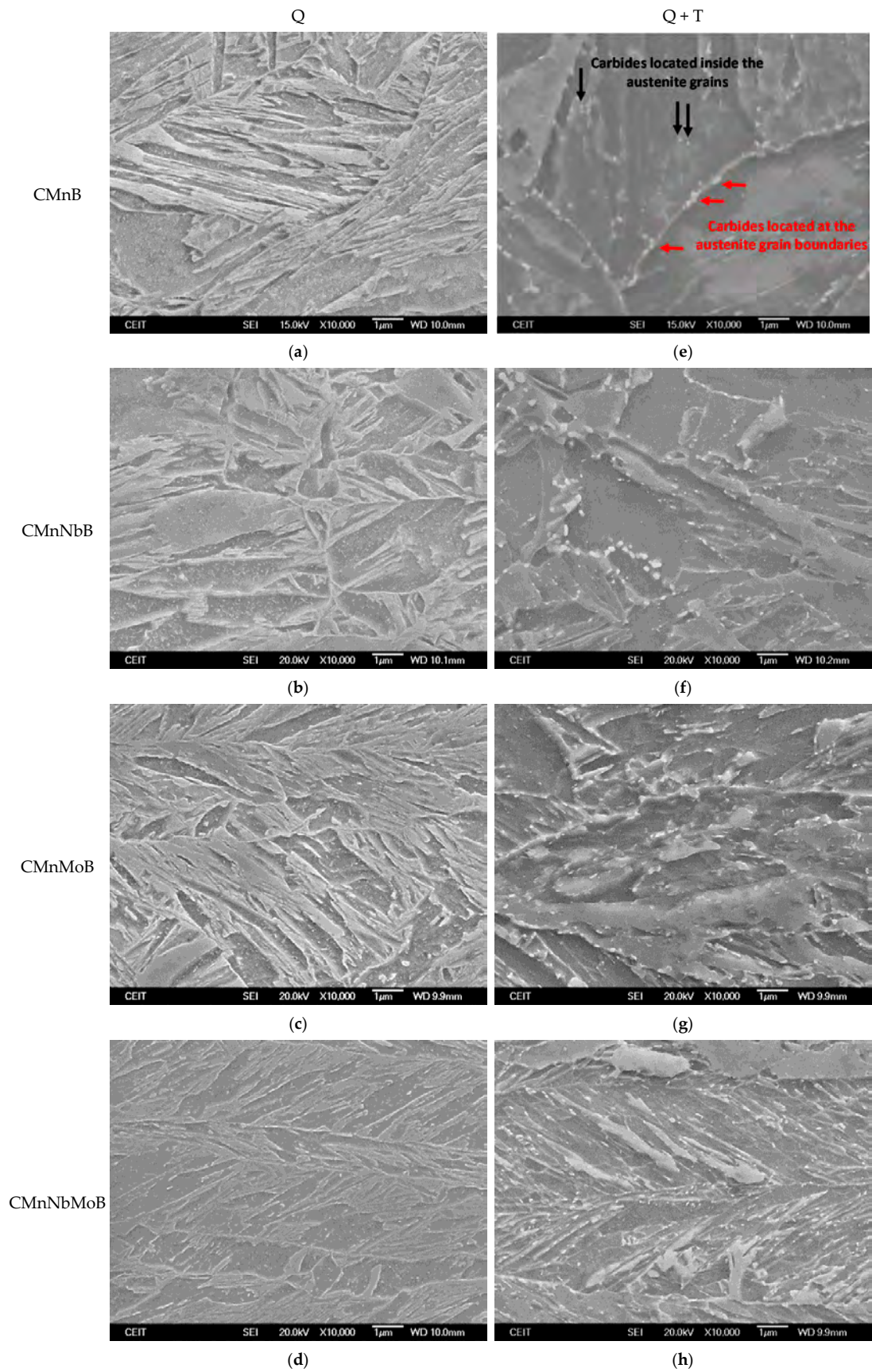


Figure 3. FESEM micrographs corresponding to (a–d) Q and (e–h) Q+T conditions for (a,e) CMnB, (b,f) CMnNbB, (c,g) CMnMoB steel, and (d,h) CMnNbMoB steels.

### 3.1.1. Quantification of Unit Sizes by Means of EBSD

Besides the qualitative characterization by means of conventional observation techniques, a quantitative crystallographic characterization was carried out using EBSD technique. In Figure 4 the IPF (Inverse Pole Figure) maps corresponding to the different steels and both Q and Q + T states are presented. Regarding the effect of chemistry, the addition of microalloying elements promotes microstructural refinement. The coarsest martensitic structure is observed in the CMnB grade before and after tempering (see Figure 4a,e). The formation of a very fine martensitic microstructure is observed in the Mo containing steels (Figure 4c,d,g,h). Moreover, the EBSD maps corresponding to Mo and NbMo micro-alloyed steels show that the transformation takes place from a heavily deformed austenitic structure, as the prior austenite pancaked structure is clearly reflected. In order to confirm this fact, samples were etched by picric acid and completely different austenite conditioning could be identified depending on the chemical composition as shown in a previous study [22]. In the CMnB steel, an equiaxed and homogeneous austenite grain structure is observed. For the CMnNbB steel, a mixed structure consisting of pancaked and dynamically recrystallized fine grains is found. The Mo containing grades comprise a fully pancaked austenite microstructure showing a high degree of strain accumulation [22]. Tempering of the CMnB steel modifies the microstructure to slightly coarser grain size as compared to the quenched state (Figure 4a,e). On the contrary, the microstructure of the micro-alloyed steels appears not to be altered by the tempering treatment (see Figure 4). This can be related to the well-known potency of Mo and Nb of strongly obstructing recrystallization at temperatures below 650 °C.

In Figure 5, the grain boundary maps related to (a,c) CMnB and (b,d) CMnMoB steels are shown. Low angle boundaries, between 2 and 15° are drawn in red, whereas the high angle boundaries, higher than 15° are represented in black. The influence of adding Mo is evidently reflected in Figure 5. Significantly finer microstructures are being achieved when Mo is added, considering both misorientation criteria. Additionally, Mo alloying augments the low angle boundary density (drawn in red), in the quenched steel and retains it even during tempering (Figure 5b,d). On the contrary, tempering of the CMnB steel evidently results in a significant reduction of the low angle boundary density (Figure 5a,c). Additionally, a slight coarsening of the microstructure for the CMnB steel is observed during the heat treatment.

The unit sizes were quantitatively determined from these EBSD scans in both, Q and Q + T states, for all steel grades. For quantifying the mean grain size, different misorientation criteria were considered, measuring the unit sizes with low and high tolerance angles. The effective grain size was calculated as the equivalent circle diameter corresponding to the individual grain area. In Figure 6, the mean grain size considering low and high angle misorientation criteria (boundaries between 2° and 15° and boundaries higher than 15°, respectively) are plotted for Q and Q + T states. Regarding the evolution of 2° mean unit size, for both Q and Q + T samples, slightly finer  $D_{2^\circ}$  are achieved when microalloying elements are added. Considering the high angle boundary misorientation criteria, a similar trend is detected. The addition of microalloying elements causes a reduction of mean unit sizes, and largely prevents coarsening by the tempering treatment. Such coarsening, however, occurs in the CMnB steel where  $D_{2^\circ}$  increases from 1.08 in the quenched state to 1.26  $\mu\text{m}$  after tempering. The NbMo steel comprises the smallest  $D_{2^\circ}$  unit size of around 0.87  $\mu\text{m}$  in Q as well as Q + T condition.

### 3.1.2. Dislocation Density Estimation Based on Kernel Average Misorientation

The impact of tempering treatment and chemical composition on the Kernel Average Misorientation (KAM) maps is compared in Figure 7 for the CMnB and CMnNbMoB grades. KAM is widely employed for dislocation density evaluation [12,24]. Regarding the effect of chemistry, the addition of microalloying elements leads to the increment of KAM values. For the Q condition, KAM value increases from 1.2° to 1.35°, when Nb and Mo are added (see Figure 7a,c).

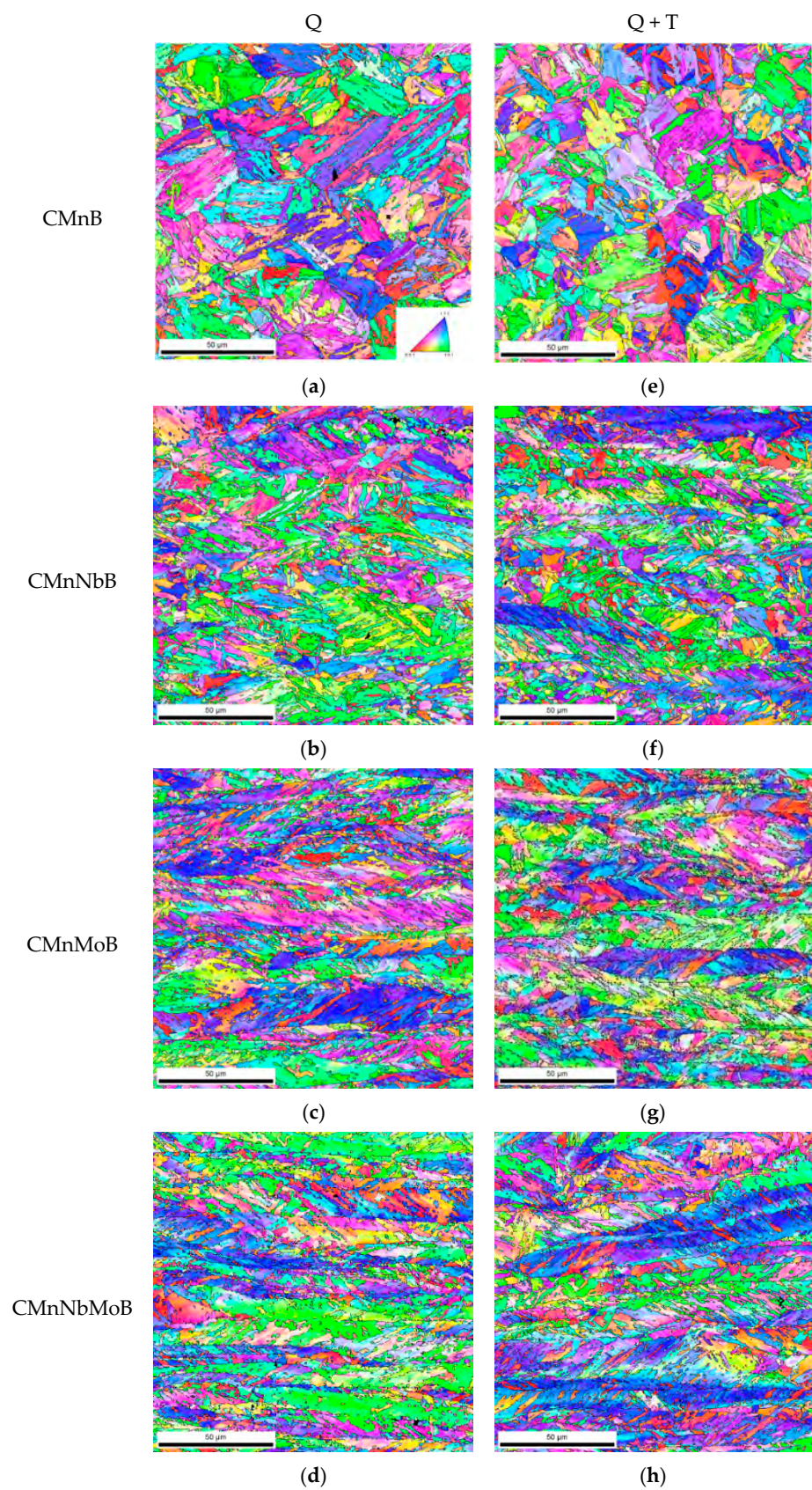


Figure 4. Inverse Pole Figure (IPF) maps corresponding to (a-d) Q and (e-h) Q + T states.



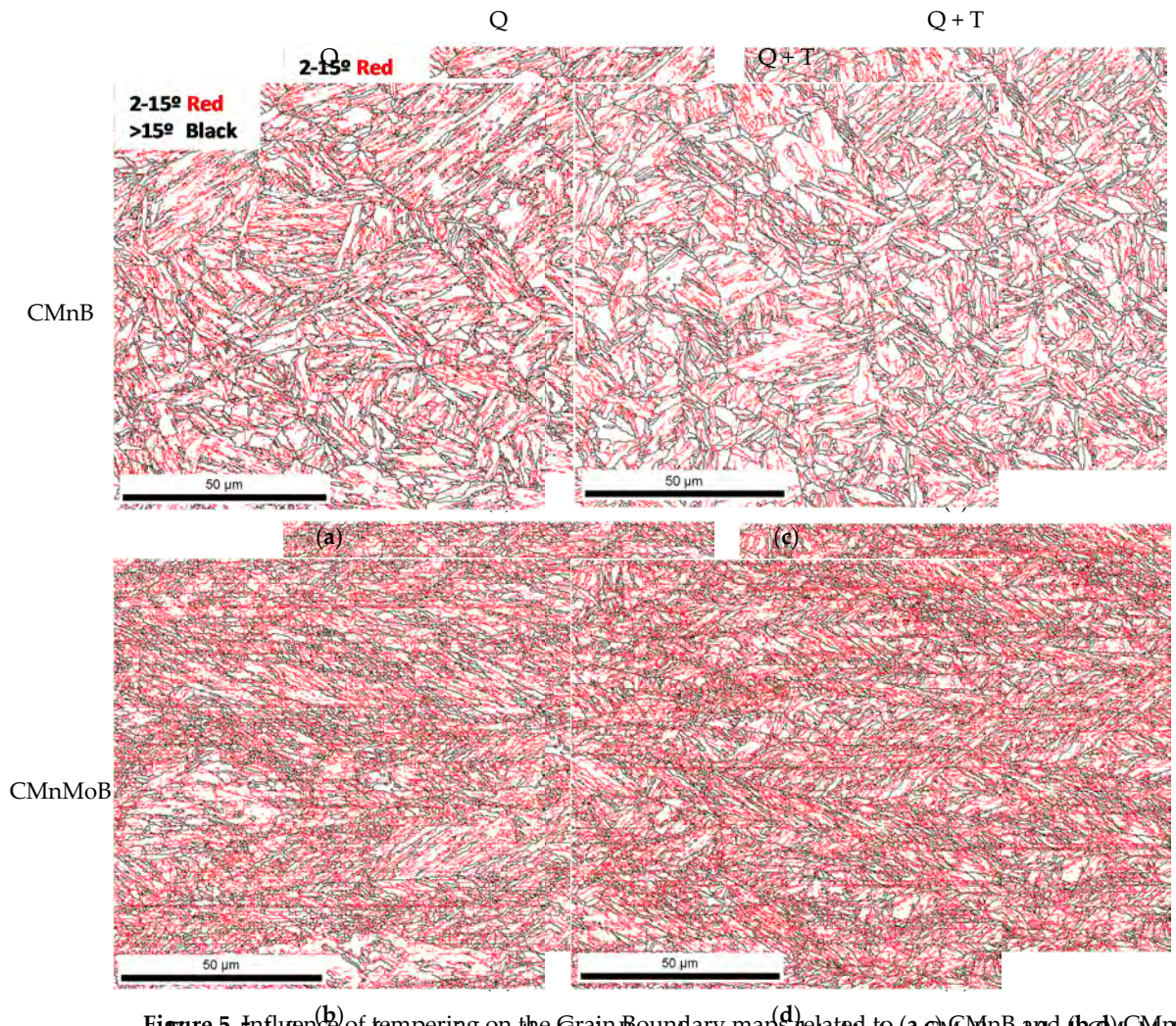


Figure 5. Influence of tempering on the Grain Boundary maps related to (a,c) CMnB and (b,d) CMnMoB.  
 Figure 5. Influence of tempering on the Grain Boundary maps related to (a,c) CMnB and (b,d) CMnMoB.

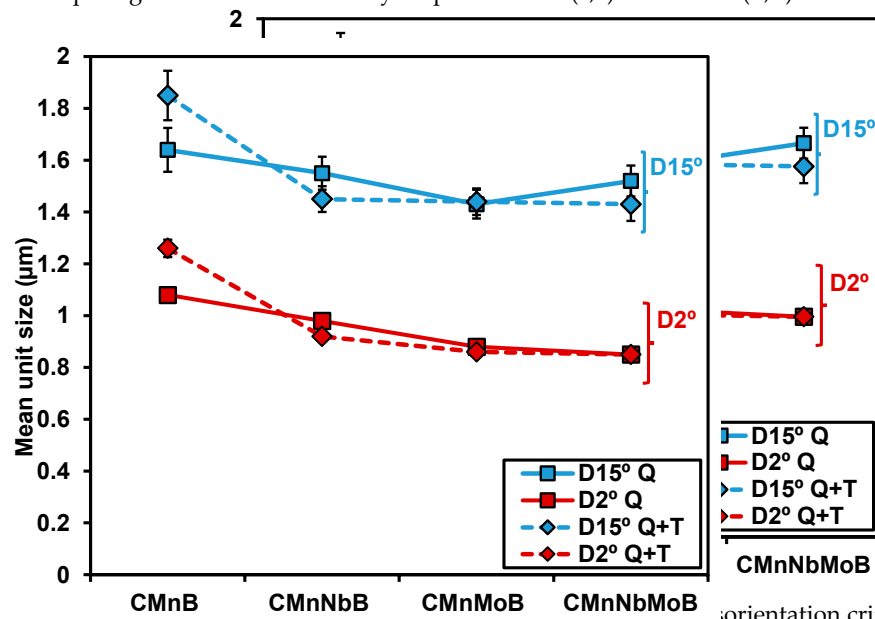
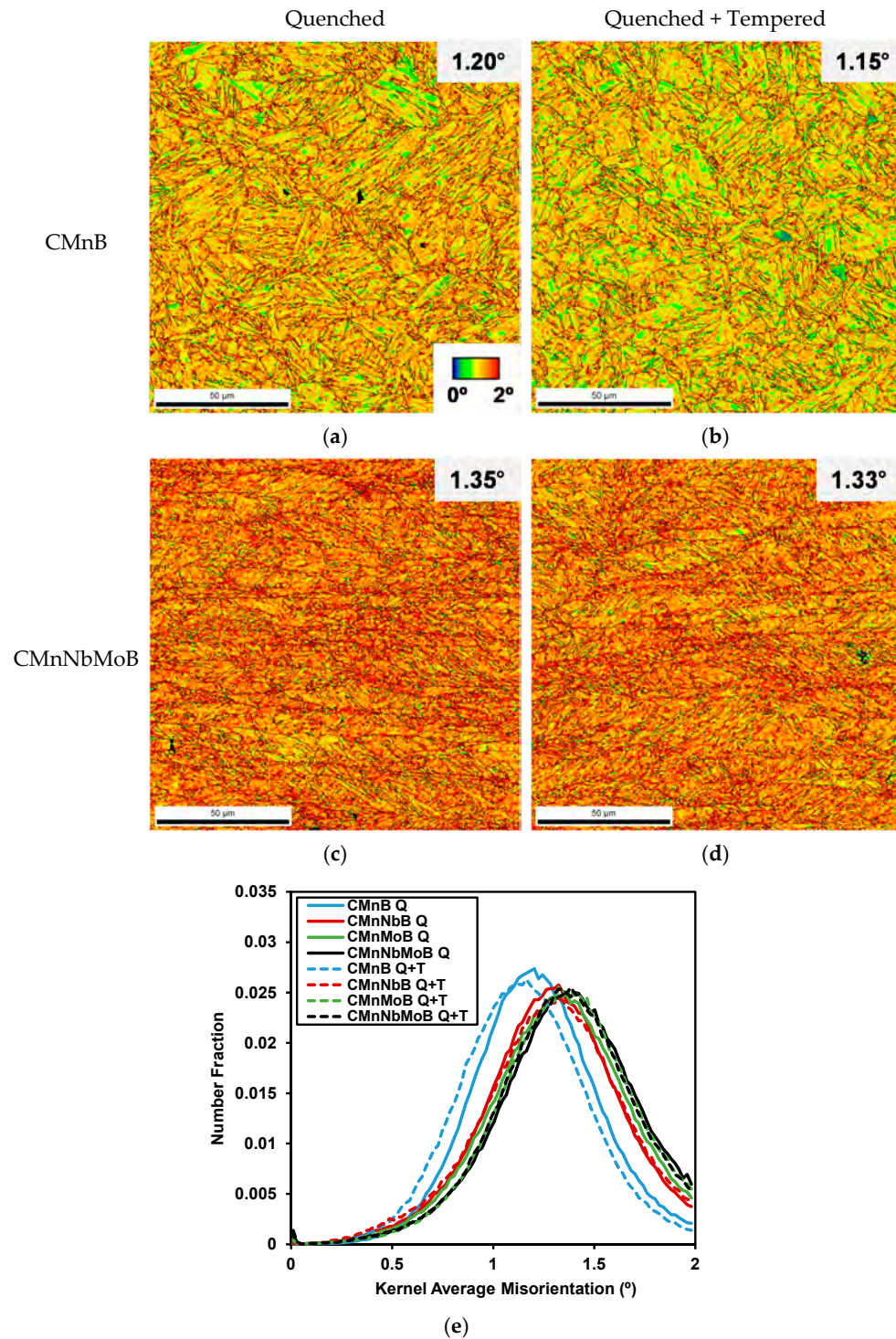


Figure 6. Mean Unit Sizes considering different misorientation criteria (tolerance angle of 2° and 15°) for both conditions: Q and Q+T cycles.  
 Figure 6. Mean Unit Sizes considering different misorientation criteria (tolerance angle of 2° and 15°) for both conditions: Q and Q+T cycles.

3.1.2. Dislocation Density estimation based on Kernel Average Misorientation

The impact of tempering treatment and chemical composition on the Kernel Average Misorientation (KAM) maps is compared in Figure 7 for the CMnB and CMnNbMoB grades. KAM is widely employed for dislocation density evaluation [12,24]. Regarding the effect of chemistry, the addition of microalloying elements leads to the increment of KAM values. For the Q condition, KAM value increases from 1.2° to 1.35°, when Nb and Mo are added (see Figure 7a,c).



**Figure 7.** Kernel Average Misorientation maps corresponding to different steels ((a,b) CMnB and (c,d) CMnNbMoB) and both conditions: (a,c) Q and (b,d) Q + T states. (e) KAM distributions corresponding to all the steel grades and both states. (c,d) CMnNbMoB) and both conditions: (a,c) Q and (b,d) Q + T states. (e) KAM distributions corresponding to all the steel grades and both states.

Analyzing the effect of tempering treatment, different behavior is noticed depending on the chemical composition. In the CMnB steel, slightly different KAM maps are observed when Q and Q + T states are compared (see Figure 7a,b). For the CMnNbMoB though, KAM parameter remains unmodified. Similar average KAM values are measured before and after heat treatment (see Figure 7c,d, KAM values of approximately 1.3°). For CMnNbB steel, similar KAM values are quantified for both conditions (of 1.28°), while for CMnMoB

grade, KAM values of  $1.30^\circ$  and  $1.34^\circ$  are measured, for Q and Q + T, respectively. Besides the average value, the effect of tempering on the KAM distributions are plotted in Figure 7e for all the steels. No impact of tempering is observed on Kernel Average Misorientation distributions for the micro-alloyed steels (Nb, Mo, and Nb-Mo). In the CMnB grade meanwhile, the tempering treatment slightly shifts the KAM distribution to lower values. The Kernel map in the Q state presents more regions in red-orange colors and the Q + T image shows some blue-green areas (see Figure 7a,b).

### 3.1.3. Fine Precipitation Analysis on Mo Containing Steels and Q + T State by TEM

Niobium, titanium, boron, and molybdenum have the potential of precipitating as carbides or nitrides. When such precipitates are formed in the bcc lattice, they can add to strength depending on particle size and amount. Titanium being a strong nitride former is added in the current quenchable steels mainly to protect boron from forming nitrides. Considering the Ti:N ratios in the current steels, most of the added Ti is tied as insoluble TiN particles. It is well-established that part of the added Nb co-precipitates with TiN particles and is thus not available for its actually intended metallurgical effects. Such TiN and Ti,Nb(C,N) precipitates typically have a coarse size and do not contribute to strength. TiN particles with cubic morphology having sizes up to the lower micrometer range could be detected in all current steels.

TEM analysis of replicas from both Mo-alloyed steels (CMnMoB and CMnNbMoB) after tempering revealed the presence of coarser-sized precipitates with complex composition. For the CMnMoB grade, these precipitates are carbo-nitrides rich in Ti and Mo, while for the CMnNbMoB steel the precipitates are rich in Ti-Mo-Nb. In some cases, co-precipitation is also observed, where the nucleation of smaller carbonitride (rich in Nb and small fraction of Ti, Mo) is detected on pre-existing TiN particles.

A population of fine-sized precipitates having diameters of less than 10 nm is detected in the CMnMoB and CMnNbMoB steels, as shown in Figure 8a,b, respectively. For the CMnNbMoB steel (Figure 8b,c), the share of fine precipitates appears to be higher and sizes below 5 nm are found. These particles are rich in Mo as indicated by the XPS spectrum in Figure 8c. The quenched condition does not allow precipitation of Mo for kinetic reasons contrary to the tempering condition. A variety of Mo containing carbide phases can be formed during tempering depending on time and temperature as well as Mo concentration [25]. The latter is not homogeneous as Mo is usually segregated to prior austenite grain boundaries where it was found to have concentration peaks in the order of 3 times the average bulk concentration [4,26]. Furthermore, Mo can segregate to substructure boundaries during tempering. Under the current tempering condition, the Mo diffusion range is limited to below 30 nm, thus not allowing strong concentration enhancement. The observed fine-sized precipitates are likely represented by MC and M<sub>2</sub>C type. MC type particles are typical for the microalloying elements Nb and Ti of which small amounts can still be solute at the onset of tempering in the present steels. It has been demonstrated that Mo clusters can nucleate such MC carbides, even representing the dominant fraction when these MC particles are ultra-fine in size [27]. The synergetic effects of molybdenum refining the size of the micro-alloy precipitates and simultaneously enhancing the MC particle volume fraction has also been reported [11,13]. M<sub>2</sub>C grows at the expense of cementite (M<sub>3</sub>C) that has previously formed at lower temperatures. Upon long tempering times M<sub>2</sub>C type particles adopt a needle-shaped morphology [28,29], which due to the short tempering are not seen in the present steels. On the other hand, Mo can participate in coarser-sized particles of type M<sub>6</sub>C or M<sub>23</sub>C<sub>6</sub> located near to M<sub>3</sub>C particles at both, large and small angle boundaries [25].

in coarser-sized particles of type  $M_6C$  or  $M_{23}C_6$  located near to  $M_3C$  particles at both, large and small angle boundaries [25].

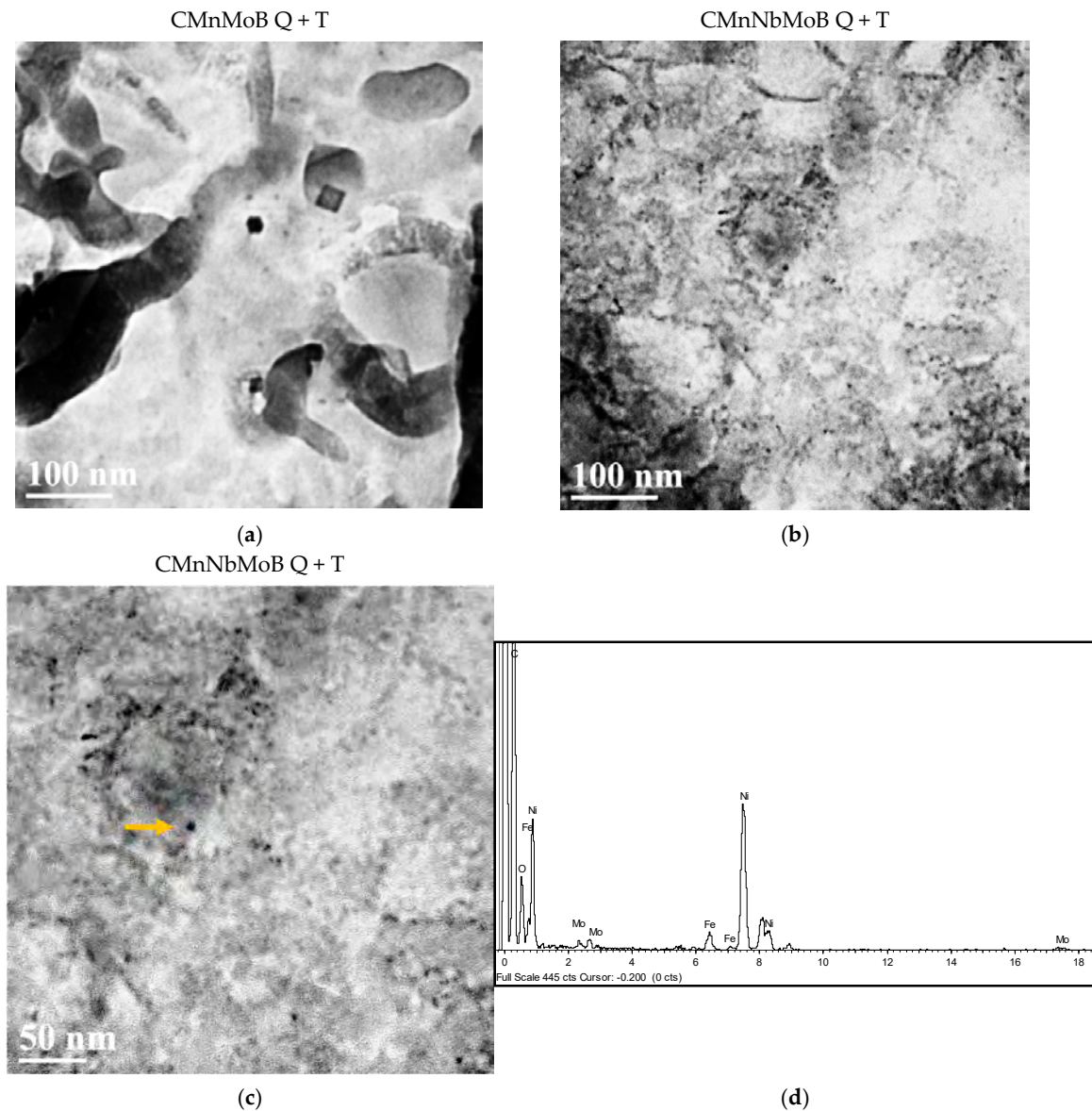


**Figure 8:** TEM micrographs corresponding to (a) CMnMoB and (b,c) CMnNbMoB grades and Q + T state (d) Microanalysis of the fine precipitate marked in (c) (the presence of Ni in the spectrum originates from the grid holding the carbon replica).

### 3.2. Interaction between Microstructure and Tensile Properties

#### 3.2. Interaction between Microstructure and Tensile Properties

##### 3.2.1. Hardness Measurements

Figure 9 compares average Vickers hardness values obtained for each chemical composition before and after tempering treatment. Considering first the quenched condition, the CMnB steel comprises the lowest hardness as expected. The sole addition of Nb and Mo raises the hardness by 16.2 HV and 45.2 HV, respectively. However, combined alloying of Nb and Mo does not result in further significant hardness increase over the Mo-only addition. Tempering generally leads to a major loss of hardness. The hardness drop is largest in the CMnB steel amounting to 187 HV. The additions of Nb and Mo reduce the hardness loss to 163 HV and 131 HV, respectively. The additions of Nb and Mo reduce the hardness loss to 163 HV and 131 HV, respectively. The combined addition of Mo and Nb further reduces the hardness loss to 114 HV. Accordingly, beyond the individual contributions of Nb and Mo to tempering resistance a significant synergetic effect is observed when both alloying elements are combined.

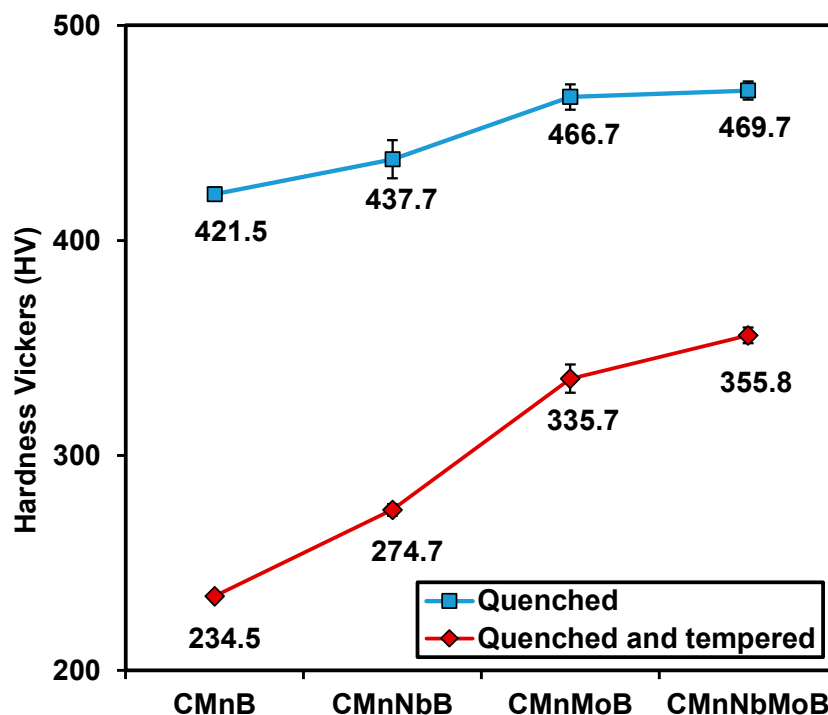


Figure 9. Hardness measurements for all steel grades for Q and Q + T cycles.

### 3.2.2. Tensile Properties

The tensile behavior of the quenched steels shows “round-house” curves with high and continuous work hardening immediately after yielding as typically observed for martensitic steels (Figure 10). The CMnB steel has the lowest strength and largest total elongation. The steels with Mo addition reach the highest strength level of over 1400 MPa tensile strength (Table 3). The Mo and Nb combined alloyed steel not only comprises the highest strength but also shows better total elongation than the steels alloyed with either Nb or Mo. The steels with Mo addition reach the highest tensile strength level is significantly reduced to values in the range of 700 to 1034 MPa, depending on the alloy concept. The strength reduction comes along with improvement of total elongation except for the Mo + Nb steel, showing lower elongation than the steels alloyed with Nb or Mo. Tempering drastically changes the tensile behavior (Figure 11). The yield-to-tensile ratio (YTR) is in the range of 0.75 to 0.95 reflecting the good work hardening potential in the quenched condition. Tempering affects the tensile strength much more than the yield strength. Accordingly, the YTR increases to values between 0.88 and 0.95. The Mo alloyed steels have the highest YTR after tempering, regardless of whether Nb is added or not. The losses in yield and tensile strength observed between the various alloys are manifested in the extent of post-uniform elongation after tempering. The yield-to-tensile ratio of 0.75 to 0.78 reflecting the good work hardening potential in the quenched condition. Tempering affects the tensile strength much more than the yield strength. The YTR increases to values between 0.88 and 0.95. The Mo alloyed steels have the highest YTR after tempering, regardless of whether Nb is added or not. The losses in yield and tensile strength observed between the various alloys are manifested in the extent of post-uniform elongation after tempering. The yield-to-tensile ratio of 0.75 to 0.78 reflecting the good work hardening potential in the quenched condition. Tempering affects the tensile strength much more than the yield strength. The YTR increases to values between 0.88 and 0.95. The Mo alloyed steels have the highest YTR after tempering, regardless of whether Nb is added or not. The losses in yield and tensile strength observed between the various alloys are manifested in the extent of post-uniform elongation after tempering. The yield-to-tensile ratio of 0.75 to 0.78 reflecting the good work hardening potential in the quenched condition.

Particularly the higher carbide fraction located at low angle boundaries has the potential of generating microstructural damage during the work hardening phase making post-uniform yielding less stable. Additionally, it must be taken into account that the stress level at the end of the work hardening phase in these steels is also significantly higher, promoting the high YTRs suggested that Mo not only provides high tempering resistance but also recovers strength by secondary hardening as well yet it has clearly lower tempering resistance as compared to the Nb added steels. The lower post-uniform elongation after tempering in the Mo and/or Nb could be related to the carbide particle population described in Section 3.1. Particularly the higher carbide fraction located at low angle boundaries has the potential of generating

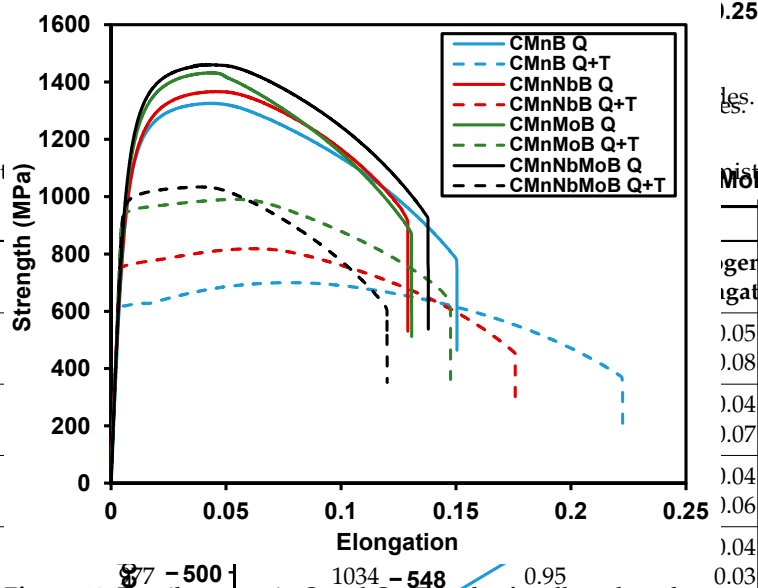
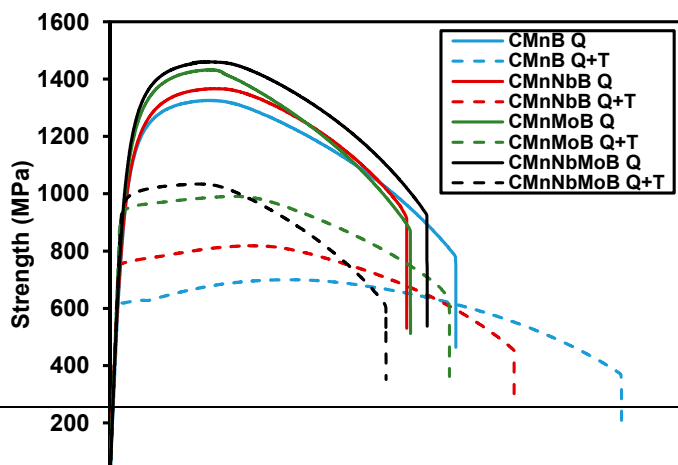


Figure 10. Tensile curves in Q and Q+T cycles for all steel grades.

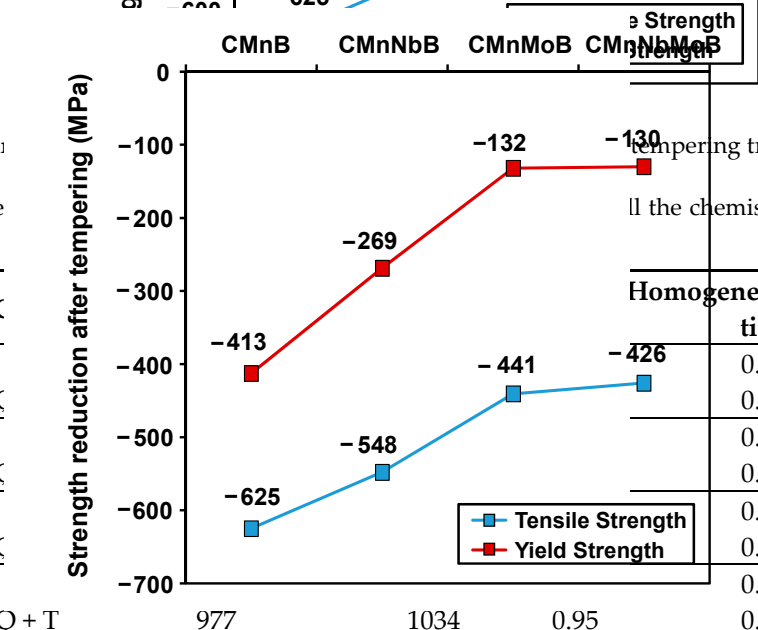


Figure 11. Reduction of yield strength and tensile strength after tempering treatment.

Metals 2021, 11, x FOR PEER REVIEW

14 of 21

Table 3. Tensile properties (ratio).

Steel	Cycle
CMnB	Q
	Q+T
CMnNbB	Q
	Q+T
CMnMoB	Q
	Q+T
CMnNbMoB	Q
	Q+T

Table 3. Tensile properties (YTR: yield-to-tensile ratio).

Chemistry	YTR	Homogeneous Elongation	Total Elongation
CMnB	0.05	0.05	0.15
CMnB	0.08	0.08	0.22
CMnNbB	0.04	0.04	0.12
CMnNbB	0.07	0.07	0.17
CMnMoB	0.04	0.04	0.13
CMnMoB	0.06	0.06	0.15
CMnNbMoB	0.04	0.04	0.14
CMnNbMoB	0.03	0.03	0.12

Table 3. Tensile properties (ratio).

Steel	Cycle	Yield Strength (MPa)	Tensile Strength (MPa)	YTR	Homogeneous Elongation	Total Elongation
CMnB	Q	977	1034	0.95	0.05	0.15
	Q+T	625	548	0.95	0.08	0.22
CMnNbB	Q	413	441	0.93	0.04	0.12
	Q+T	269	426	0.93	0.07	0.17
CMnMoB	Q	413	441	0.93	0.04	0.13
	Q+T	269	426	0.93	0.06	0.15
CMnNbMoB	Q	413	441	0.93	0.04	0.14
	Q+T	269	426	0.93	0.03	0.12

Table 3. Tensile properties (YTR: yield-to-tensile ratio).

Table 3. Tensile properties (YTR: yield-to-tensile ratio).

Chemistry	YTR	Homogeneous Elongation	Total Elongation
CMnB	0.05	0.05	0.15
CMnB	0.08	0.08	0.22
CMnNbB	0.04	0.04	0.12
CMnNbB	0.07	0.07	0.17
CMnMoB	0.04	0.04	0.13
CMnMoB	0.06	0.06	0.15
CMnNbMoB	0.04	0.04	0.14
CMnNbMoB	0.03	0.03	0.12

Table 3. Tensile properties measured before and after tempering treatment for all the chemistries (YTR: yield-to-tensile ratio).

Steel	Cycle	Yield Strength (MPa)	Tensile Strength (MPa)	YTR	Homogeneous Elongation	Total Elongation
CMnB	Q	977	1034	0.95	0.05	0.15
	Q+T	625	548	0.95	0.08	0.22
CMnNbB	Q	413	441	0.93	0.04	0.12
	Q+T	269	426	0.93	0.07	0.17
CMnMoB	Q	413	441	0.93	0.04	0.13
	Q+T	269	426	0.93	0.06	0.15
CMnNbMoB	Q	413	441	0.93	0.04	0.14
	Q+T	269	426	0.93	0.03	0.12

### 3.3. Estimation of the Contribution of Strengthening Mechanisms on Yield Strength

Based on the information obtained from the EBSD characterization, the contribution of different strengthening mechanisms to yield strength was estimated for all investigated conditions. The yield strength of low carbon micro-alloyed steel grades can be calculated considering a linear sum of individual strengthening mechanisms, such as solid solution ( $\sigma_{ss}$ ), unit size refinement ( $\sigma_{gs}$ ), and dislocation density ( $\sigma_{\rho}$ ) according to Equation (1). For martensitic microstructures, however, a further contribution termed “unaccounted strength” ( $\sigma_{us}$ ) must be added. This contribution accounts for the effect of carbon in solid solution. In this study, the individual contributions of the each strengthening mechanisms have been estimated by means of different approaches reported in the literature (see the summary of the used equations in Table 4).

$$\text{Yield Strength (MPa)} = \sigma_{ss} + \sigma_{gs} + \sigma_{\rho} + \sigma_{us} \quad (1)$$

**Table 4.** Summary of the used equations for estimating the contribution of different strengthening mechanisms.

<b>Solid Solution</b>	$\sigma_{ss} = \sigma_0 + 32.3(\%Mn) + 83.2(\%Si) + 11(\%Mo) + 354(\%N_{free})^{0.5}$	[30]
<b>Grain Size</b>	$\sigma_{gs} = 1.05\alpha M\mu\sqrt{b} \left[ \sum_{2 \leq \theta_i \leq 15^\circ} f_i \sqrt{\theta_i} + \sqrt{\frac{\pi}{10}} \sum_{\theta_i \geq 15^\circ} f_i \right] d_{2^\circ}^{-\frac{1}{2}}$	[31]
<b>Dislocation Density</b>	$\rho = \frac{2\theta}{u \cdot b}, \sigma_{\rho} = \alpha M\mu b\sqrt{\rho}$	[24,32]

The effect of solid solution was calculated by means of the equation proposed by Pickering [31] (see Table 4). For martensitic microstructures, the contribution of microstructural refinement has been extensively estimated in the literature by considering the Hall–Petch type relationships [5]. However, there is no unanimity in the definition of the effective grain size acting as an obstacle on dislocation movement in a martensitic matrix. Some authors consider the packet size as the effective gain size in lath martensite [33,34], while other works state that block size controls the strength [35,36]. Hannula et al. [37] showed that the effective grain size can be determined by measuring high angle misorientation boundaries (higher than 15°) through EBSD technique and they concluded that its square root correlates well with the measured yield strength. The equation proposed by Iza-Mendia et al. [31], where both types of boundaries (low and high angle) are considered and balanced by their fraction (see Table 4) is the approach selected in the present analysis. This approach was validated for a wide range of microstructures (ferritic-pearlitic, bainitic and martensitic microstructures). Low and high angle boundary fractions ( $f_i$ ), as well as mean unit size considering low angle misorientation criteria ( $d_{2^\circ}$ ) were calculated by EBSD technique for the different steel grades and both states. Finally, hardening due to dislocation density was evaluated through Kernel Average Misorientation obtained by EBSD scans, according to the equations shown in Table 4 [24,32]. More details regarding the considered assumptions as well as the followed procedure can be found in Refs. [12,38].

For estimating the contribution of unaccounted strength ( $\sigma_{us}$ ), the difference between the experimental yield strength (measured by tensile tests) and the rest of the terms (related to solid solution, grain size refinement, and dislocation density) was calculated. For the quenched state,  $\sigma_{us}$  is associated with the impact the carbon in solid solution, while for tempered state, this term can also account for the strengthening effect of nanosized precipitates formed by Nb and Mo during tempering treatment.

In Table 5 and Figure 12a,b, the values for the different strengthening mechanisms are shown for both Q and Q + T conditions, respectively. For verification, the experimental yield strength values obtained by tensile tests are represented by the red dots in the figure. Regarding the quenched state, similar contribution due to solid solution are estimated

for all the steels. The results suggest that the most relevant strengthening mechanism is associated with the unit sizes. Contributions ranging from 472 to 528 MPa are quantified, for CMnB and CMnNbMoB steels, respectively. No significant effect on the hardening related to dislocation density is apparent from adding microalloying elements as this contribution only increases from 114 to 121 MPa at the most. The hardening due to carbon in solid solution is associated in the unaccounted strength ( $\sigma_{us}$ ), as explained earlier. This contribution is calculated as the difference between experimental yield strength and the sum of all other contributions. Values higher than 300 MPa are quantified in all the cases for the unaccounted strength ( $\sigma_{us}$ ). A similar procedure was also considered in other works [39].

**Table 5.** Individual contributions of strengthening mechanism to yield strength.

Steel	Cycle	Solid Solution (MPa)	Grain Size (MPa)	Dislocation Density (MPa)	Unaccounted Strength (MPa)
CMnB	Q	115	472	114	329
CMnNbB	Q	112	496	118	300
CMnMoB	Q	117	516	119	323
CMnNbMoB	Q	120	528	121	338
CMnB	Q+T	115	448	112	11
CMnNbB	Q+T	112	516	118	11
CMnMoB	Q+T	117	520	121	185
CMnNbMoB	Q+T	120	508	120	229

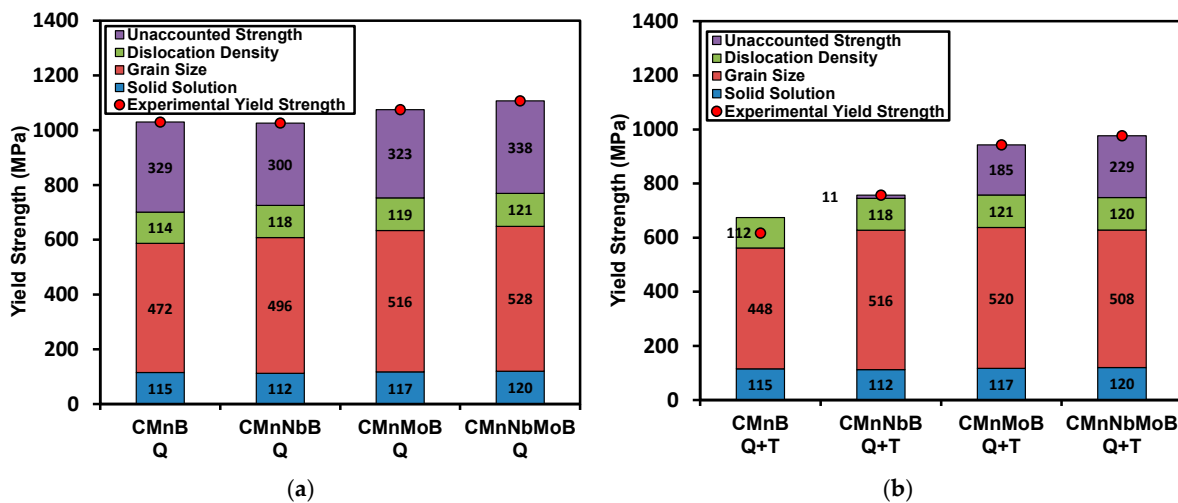


**Figure 12.** Contribution of different strengthening mechanisms (solid solution, grain size, dislocation density and unaccounted strength) to the yield strength: (a) Q and (b) Q + T states.

The contributions of individual strengthening mechanisms to yield strength after tempering treatment are presented in Figure 12b. No considerable impact of the tempering treatment is seen for the contributions by solid solution, unit size and dislocation density. In CMnB steel, the unit size contribution is estimated to be slightly lower after tempering, due to the observed coarsening of the microstructure (see Figures 5 and 6). The experimentally observed yield strength drop after tempering is predominantly controlled by the unaccounted strength term and in this respect, molybdenum displays its marked effect of tempering resistance as already mentioned earlier. For the CMnB and Nb-only alloyed steel the unaccounted strength drops to a marginal level after tempering. This can be associated with the thermally activated diffusion of carbon during tempering and the lack of carbon in interstitial solution remaining after tempering in the CMnB and CMnNbB steels. Conversely, in the Mo-bearing steels, a high contribution of the unaccounted strength

The contributions of individual strengthening mechanisms to yield strength after tempering treatment are presented in Figure 12b. No considerable impact of the tempering treatment is seen for the contributions by solid solution, unit size and dislocation density. In CMnB steel, the unit size contribution is estimated to be slightly lower after tempering, due to the observed coarsening of the microstructure (see Figures 5 and 6). The







Upon tempering (600 °C/900 s), the CMnB steel experiences a large drop of yield and tensile strength in the order of 400 MPa and 600 MPa, respectively. The CMnNbMoB steel, however, still meets the minimum required specified tensile properties.

The excellent tempering resistance in the CMnNbMoB steel can be due to individual and synergetic effects by molybdenum and niobium. Detailed EBSD analysis revealed that the small niobium addition is highly efficient in retaining the extremely fine large-angle and small-angle unit sizes present in the quenched condition during tempering, while the CMnB steel shows measurable coarsening of these. Molybdenum alloying establishes a particularly fine-sized low-angle grain boundary structure in the quenched steel that is retained even after tempering.

The strength loss caused by redistribution and precipitation of interstitial carbon during tempering accounts for approximately 320 MPa in all investigated steels. A major part of that strength loss is compensated by precipitation strengthening in the Mo-alloyed steels. Ultra-fine Mo-rich precipitates have been identified by TEM. Experimental data and theoretical estimations suggest that precipitation strengthening accounts for approximately 200 MPa gain in yield strength. While the small available amount of Nb by itself contributes only around 10 MPa to precipitation strengthening, the synergy between Mo and Nb adds around 50 MPa over the Mo-only effect.

The presence of ultra-fine precipitates and their particularly strong effect on yield strength reflects in a very high yield-to-tensile ratio of 0.95 after tempering. Nevertheless, the Mo-alloyed steels maintain continuous yielding after tempering whereas the CMnB steel shows features of Lüders elongation.

**Author Contributions:** I.Z. carried out the experiments and wrote the manuscript; N.I. supervised the results, analyzed the data and wrote the manuscript; E.D., V.S. and H.M. contributed to the interpretation of the data and edited the manuscript; P.U. managed the project and edited the manuscript. All authors have read and agreed to the published version of the manuscript.

**Funding:** This research received funding by the International Molybdenum Association (IMOA).

**Institutional Review Board Statement:** Not applicable.

**Informed Consent Statement:** Not applicable.

**Data Availability Statement:** Data sharing not applicable.

**Acknowledgments:** The authors would like to acknowledge the International Molybdenum Association (IMOA) for funding this project.

**Conflicts of Interest:** The authors declare no conflict of interest.

## References

1. Llewellyn, D.T. Nitrogen in Steels. *Ironmak. Steelmak.* **1993**, *20*, 338–343.
2. Taylor, K.A. Grain-boundary segregation and precipitation of boron in 0.2 percent carbon steels. *Met. Mater. Trans. A* **1992**, *23*, 107–119. [[CrossRef](#)]
3. Shigesato, G.; Fujishiro, T.; Hara, T. Grain Boundary Segregation Behavior of Boron in Low-Alloy Steel. *Met. Mater. Trans. A* **2014**, *45*, 1876–1882. [[CrossRef](#)]
4. Li, Y.; Ponge, D.; Choi, P.; Raabe, D. Segregation of boron at prior austenite grain boundaries in a quenched martensitic steel studied by atom probe tomography. *Scr. Mater.* **2015**, *96*, 13–16. [[CrossRef](#)]
5. Mohrbacher, H. Property Optimization in As-Quenched Martensitic Steel by Molybdenum and Niobium Alloying. *Metals* **2018**, *8*, 234. [[CrossRef](#)]
6. Larrañaga-Otegui, A.; Pereda, B.; Jorge-Badiola, D.; Gutiérrez, I. Austenite Static Recrystallization Kinetics in Microalloyed B Steels. *Met. Mater. Trans. A* **2016**, *47*, 3150–3164. [[CrossRef](#)]
7. He, X.; Djahazi, M.; Jonas, J.; Jackman, J. The non-equilibrium segregation of boron during the recrystallization of Nb-treated HSLA steels. *Acta Met. Mater.* **1991**, *39*, 2295–2308. [[CrossRef](#)]
8. Hulka, K.; Kern, A.; Schriever, U. Application of Niobium in Quenched and Tempered High-Strength Steels. *Mater. Sci. Forum* **2005**, *500–501*, 519–526. [[CrossRef](#)]
9. Miao, C.; Shang, C.; Zhang, G.; Subramanian, S. Recrystallization and strain accumulation behaviors of high Nb-bearing line pipe steel in plate and strip rolling. *Mater. Sci. Eng. A* **2010**, *527*, 4985–4992. [[CrossRef](#)]

10. Hutchinson, C.; Zurob, H.; Sinclair, C.; Brechet, Y. The comparative effectiveness of Nb solute and NbC precipitates at impeding grain-boundary motion in Nb steels. *Scr. Mater.* **2008**, *59*, 635–637. [[CrossRef](#)]
11. Isasti, N.; Jorge-Badiola, D.; Taheri, M.L.; Uranga, P. Microstructural and precipitation characterization in Nb-Mo microalloyed steels: Estimation of the contributions to the strength. *Met. Mater. Int.* **2014**, *20*, 807–817. [[CrossRef](#)]
12. Larzabal, G.; Isasti, N.; Rodriguez-Ibabe, J.; Uranga, P. Evaluating Strengthening and Impact Toughness Mechanisms for Ferritic and Bainitic Microstructures in Nb, Nb-Mo and Ti-Mo Microalloyed Steels. *Metals* **2017**, *7*, 65. [[CrossRef](#)]
13. Lee, W.-B.; Hong, S.-G.; Park, C.-G.; Park, S.-H. Carbide precipitation and high-temperature strength of hot-rolled high-strength, low-alloy steels containing Nb and Mo. *Met. Mater. Trans. A* **2002**, *33*, 1689–1698. [[CrossRef](#)]
14. Togashi, F.; Nishizawa, T. Effect of Alloying Elements on the Mobility of Ferrite/Austenite Interface. *J. Jpn. Inst. Met.* **1976**, *40*, 12–21. [[CrossRef](#)]
15. Coldren, A.P.; Eldis, G.T. Using CCT Diagrams to Optimize the Composition of an As-Rolled Dual-Phase Steel. *JOM* **1980**, *32*, 41–48. [[CrossRef](#)]
16. Cizek, P.; Wynne, B.P.; Davies, C.H.J.; Hodgson, P.D. The Effect of Simulated Thermomechanical Processing on the Transformation Behavior and Microstructure of a Low-Carbon Mo-Nb Linepipe Steel. *Met. Mater. Trans. A* **2015**, *46*, 407–425. [[CrossRef](#)]
17. Isasti, N.; Jorge-Badiola, D.; Taheri, M.L.; Lopez, B.; Uranga, P. Effect of Composition and Deformation on Coarse-Grained Austenite Transformation in Nb-Mo Microalloyed Steels. *Met. Mater. Trans. A* **2011**, *42*, 3729–3742. [[CrossRef](#)]
18. Olasolo, M.; Uranga, P.; Rodriguez-Ibabe, J.; López, B. Effect of austenite microstructure and cooling rate on transformation characteristics in a low carbon Nb-V microalloyed steel. *Mater. Sci. Eng. A* **2011**, *528*, 2559–2569. [[CrossRef](#)]
19. Kaijalainen, A.J.; Suikkanen, P.; Linnell, T.J.; Karjalainen, L.P.; Kömi, J.; Porter, D.A. Effect of austenite grain structure on the strength and toughness of direct-quenched martensite. *J. Alloys Compd.* **2013**, *577*, S642–S648. [[CrossRef](#)]
20. Opiela, M.; Grzegorzczak, B. Thermo-mechanical Treatment of Forged Products of Ti-V-B Microalloyed Steel. In Proceedings of the Metal 2013, 22nd International Conference on Metallurgy and Materials, Brno, Czech Republic, 15–17 May 2013; Tanger Ltd.: Ostrava, Czechia, 2013; pp. 796–801.
21. Siwecki, T. Improving Mechanical Properties on High-Strength Steel Plate by Optimizing the Direct Quenching Process. In Proceedings of the International Symposium on the Recent Developments in Plate Steels, Winter Park, CO, USA, 19–22 June 2011.
22. Zurutuza, I.; Isasti, N.; Detemple, E.; Schwinn, V.; Mohrbacher, H.; Uranga, P. Effect of Thermomechanical Strategy and Mo-Nb-B Alloying Additions on High Strength Medium Carbon Q/Q&T Steels. In Proceedings of the Materials Science and Technology 2019 (MS&T19) Conference, Portland, OR, USA, 29 September–3 October 2019; pp. 1401–1408. [[CrossRef](#)]
23. Uranga, P.; Gutiérrez, I.; López, B. Determination of recrystallization kinetics from plane strain compression tests. *Mater. Sci. Eng. A* **2013**, *578*, 174–180. [[CrossRef](#)]
24. Calcagnotto, M.; Ponge, D.; Demir, E.; Raabe, D. Orientation gradients and geometrically necessary dislocations in ultrafine grained dual-phase steels studied by 2D and 3D EBSD. *Mater. Sci. Eng. A* **2010**, *527*, 2738–2746. [[CrossRef](#)]
25. Zhou, T.; Babu, R.P.; Hou, Z.; Odqvist, J.; Hedström, P. Precipitation of multiple carbides in martensitic CrMoV steels—Experimental analysis and exploration of alloying strategy through thermodynamic calculations. *Materialia* **2020**, *9*, 100630. [[CrossRef](#)]
26. Mohrbacher, H.; Senuma, T. Alloy Optimization for Reducing Delayed Fracture Sensitivity of 2000 MPa Press Hardening Steel. *Metals* **2020**, *10*, 853. [[CrossRef](#)]
27. Seol, J.-B.; Na, S.-H.; Gault, B.; Kim, J.-E.; Han, J.-C.; Park, C.-G.; Raabe, D. Core-shell nanoparticle arrays double the strength of steel. *Sci. Rep.* **2017**, *7*, srep42547. [[CrossRef](#)]
28. Yamasaki, S.; Bhadeshia, H.K.D.H. Modelling and characterisation of Mo<sub>2</sub>C precipitation and cementite dissolution during tempering of Fe–C–Mo martensitic steel. *Mater. Sci. Technol.* **2003**, *19*, 723–731. [[CrossRef](#)]
29. Fujita, N.; Bhadeshia, H. Precipitation of molybdenum carbide in steel: Multicomponent diffusion and multicomponent capillary effects. *Mater. Sci. Technol.* **1999**, *15*, 627–634. [[CrossRef](#)]
30. Pickering, F.B.; Gladman, T. *Metallurgical Developments in Carbon Steels*; Special Report No. 81; Iron and Steel Institute: London, UK, 1963.
31. Iza-Mendia, A.; Gutiérrez, I. Generalization of the existing relations between microstructure and yield stress from ferrite–pearlite to high strength steels. *Mater. Sci. Eng. A* **2013**, *561*, 40–51. [[CrossRef](#)]
32. Kubin, L.; Mortensen, A. Geometrically necessary dislocations and strain-gradient plasticity: A few critical issues. *Scr. Mater.* **2003**, *48*, 119–125. [[CrossRef](#)]
33. Tomita, Y.; Okabayashi, K. Effect of microstructure on strength and toughness of heat-treated low alloy structural steels. *Met. Mater. Trans. A* **1986**, *17*, 1203–1209. [[CrossRef](#)]
34. Wang, C.; Wang, M.; Shi, J.; Hui, W.; Dong, H. Effect of Microstructure Refinement on the Strength and Toughness of Low Alloy Martensitic Steel. *J. Mater. Sci. Technol.* **2007**, *23*, 659–664.
35. Morito, S.; Ohba, T. Crystallographic Analysis of Characteristic Sizes of Lath Martensite Morphology. In *Fundamentals of Martensite and Bainite toward Future Steels with High Performance*; Furuhashi, T., Tsuzaki, K., Eds.; ISIJ: Tokyo, Japan, 2007; pp. 57–62.
36. Morris, J.J.W. On the Ductile-Brittle Transition in Lath Martensitic Steel. *ISIJ Int.* **2011**, *51*, 1569–1575. [[CrossRef](#)]
37. Hannula, J.; Kömi, J.; Porter, D.A.; Somani, M.C.; Kaijalainen, A.; Suikkanen, P.; Yang, J.-R.; Tsai, S.-P. Effect of Boron on the Strength and Toughness of Direct-Quenched Low-Carbon Niobium Bearing Ultra-High-Strength Martensitic Steel. *Met. Mater. Trans. A* **2017**, *48*, 5344–5356. [[CrossRef](#)]

38. Isasti, N.; Jorge-Badiola, D.; Taheri, M.L.; Uranga, P. Microstructural Features Controlling Mechanical Properties in Nb-Mo Microalloyed Steels. Part I: Yield Strength. *Met. Mater. Trans. A* **2014**, *45*, 4960–4971. [[CrossRef](#)]
39. Hutchinson, B.; Hagström, J.; Karlsson, O.; Lindell, D.; Tornberg, M.; Lindberg, F.; Thuvander, M. Microstructures and hardness of as-quenched martensites (0.1–0.5%C). *Acta Mater.* **2011**, *59*, 5845–5858. [[CrossRef](#)]
40. Mohrbacher, H.; Yang, J.-R.; Chen, Y.-W.; Rehr, J.; Hebesberger, T. Metallurgical Effects of Niobium in Dual Phase Steel. *Metals* **2020**, *10*, 504. [[CrossRef](#)]
41. Ashby, M.F. *Physics of Strength and Plasticity*; Argon, A.S., Ed.; MIT Press: Cambridge, MA, USA, 1969; p. 113.
42. Larzabal, G.; Isasti, N.; Rodriguez-Ibabe, J.M.; Uranga, P. Precipitation Strengthening by Induction Treatment in High Strength Low Carbon Microalloyed Hot-Rolled Plates. *Met. Mater. Trans. A* **2018**, *49*, 946–961. [[CrossRef](#)]
43. Huang, B.M.; Yang, J.-R.; Yen, H.W.; Hsu, C.H.; Huang, C.Y.; Mohrbacher, H. Secondary hardened bainite. *Mater. Sci. Technol.* **2014**, *30*, 1014–1023. [[CrossRef](#)]
44. Xie, Z.; Ren, Y.; Zhou, W.; Yang, J.; Shang, C.; Misra, R. Stability of retained austenite in multi-phase microstructure during austempering and its effect on the ductility of a low carbon steel. *Mater. Sci. Eng. A* **2014**, *603*, 69–75. [[CrossRef](#)]
45. Colla, V.; De Sanctis, M.; DiMatteo, A.; Lovicu, G.; Solina, A.; Valentini, R. Strain Hardening Behavior of Dual-Phase Steels. *Met. Mater. Trans. A* **2009**, *40*, 2557–2567. [[CrossRef](#)]
46. Kamikawa, N.; Sato, K.; Miyamoto, G.; Murayama, M.; Sekido, N.; Tsuzaki, K.; Furuhashi, T. Stress–strain behavior of ferrite and bainite with nano-precipitation in low carbon steels. *Acta Mater.* **2015**, *83*, 383–396. [[CrossRef](#)]